18TH WORLD CONFERENCE ON EARTHQUAKE ENGINEERING
WCEE2024
MILAN

MILAN, ITALY
30TH JUNE - 5TH JULY 2024

www.wcee2024.it

CONSTRAINING LARGE MAGNITUDE EVENT SOURCE AND PATH EFFECTS USING GROUND MOTION SIMULATIONS

X. Meng[1], R. Graves[2] & C. Goulet[2]

[1] Statewide California Earthquake Center, Los Angeles, California, United States, xiaofenm@usc.edu

[2] United States Geological Survey, Pasadena, California, United States

Abstract: *The purpose of this study is to use ground motion simulations to investigate ways in which source and path effects for large magnitude events can be represented in non-ergodic ground motion models (GMMs). While we initially developed computation techniques using CyberShake simulations, the range of magnitudes and source-site combinations is not adequate to replicate what is observed empirically. We therefore designed a new ground motion simulation study, which includes earthquakes with a large range of magnitudes distributed uniformly on a fault plane, and sites covering a large range of rupture distances and azimuths. After running a large suite of simulations (M4-M7), we then develop a non-ergodic GMM with the simulation data. We find that the within-site residuals are dominated by the radiation pattern, rupture directivity, and slip patterns. Next, we modify an existing rupture directivity model to fit and remove the observed radiation pattern and rupture directivity from the residuals. We also minimize the contributions of slip patterns by averaging the within-site residuals among multiple source realizations. Finally, after removing the source effects from the within-site residuals, we compare the path effects computed with different magnitude groups using two approaches. The first approach only considers the small events that have the same shortest path to a site with the large events, while the second approach considers all small events on the fault plane. The results indicate that the path effects of large events cannot be satisfactorily approximated with that of small events using either approach.*

1 Introduction

In earthquake engineering design, the demand is characterized by a certain level of ground shaking, usually expressed in terms of a design response spectrum. The specific levels of performance and ground motion are generally defined by a building code with ground motions based on probabilistic seismic hazard analysis (PSHA) results. PSHA quantifies ground motions and the uncertainties in the location and magnitude of earthquakes, wave attenuation and site response that impact those ground motions (McGuire, 1995; McGuire, 2004). One principal component of PSHA is the variability of ground motions expected at a site, given a specific earthquake scenario. In practice, such variability is represented by the total standard deviation (σ_{tot}) of the residuals between ground motion measurements and the median predictions from a ground motion model (GMM).

Strasser et al. (2009) showed that σ_{tot} remained similar over four decades (1970-2010) despite substantial increase in the number of strong-motion recordings and in the complexity of the GMMs. The most promising way to reduce σ_{tot} is through the removal of the ergodic assumption, that is, assuming the variability of ground motions at one site over time equals the variability of ground motions over all sites in a short time interval. For

example, if one site has persistent large site response, it should be identified as epistemic uncertainty and removed from total variability. Similarly, wave propagation path effects between a source location and a site should be considered as repeatable, with their possible values constituting epistemic uncertainty.

There are two potential problems in estimating the path effects in current non-ergodic GMM development. First, since certain source effects (e.g., radiation pattern and rupture directivity) are a function of both earthquakes and site locations, they will likely be mapped into the path effects, which may lead to significant bias in path-specific seismic hazard assessment. Second, the path effects of small and large earthquakes are usually assumed to be the same, if their closest points on the rupture areas to the site are very close. In other words, the path effects are often assigned to a single path between the closest point and the site, regardless of the rupture area dimension. For a large earthquake, seismic waves travel from any point along the rupture plane that extends hundreds of kilometers, hence the single travel path assumption for large earthquakes may introduce significant errors in the path effects. Theoretically, we would need to include an infinite number of paths spanning from the entire area of the complex rupture plane when estimating the comprehensive path effects of large earthquakes. In reality, we need to make simplifications, such as aggregating path effects from many small earthquakes that sample the rupture area of large earthquakes.

We specifically design a ground motion simulation study to evaluate the significance of the two aforementioned shortcomings (Figure 1 and 2). We first introduce the detailed set up of the ground motion simulations. We then describe the development of non-ergodic GMM with the simulation data. We next present our main findings, which evaluate the significance of several source effects in computing the path effects and the single-path assumption for large earthquakes. We close with a discussion of these findings and their broader implications for hazard analysis.

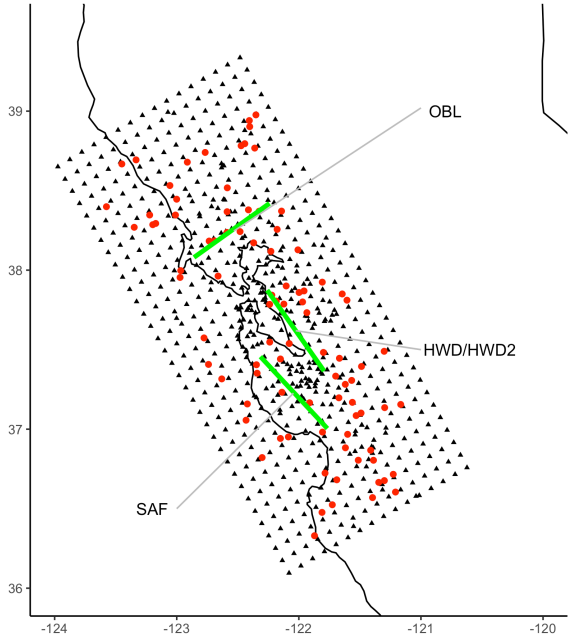

Figure 1. Map of ground motion simulation in northern California. Black triangles denote sites. Red dots denote earthquakes from NGA-West2 dataset with magnitude between 4 and 5. Green lines denote the surface projection of four faults: the San Andreas Fault (SAF), a hypothetical Oblique Fault (OBL), the Hayward Fault (HWD), and a hypothetical dipping Hayward Fault (HWD2).

2 Data and method

2.1 Ground motion simulation

Our simulations are set in northern California and include 678 sites and 854 earthquakes (Figure 1). 90 earthquakes are from the NGA-West2 dataset with magnitudes between 4 and 5 (red dots in Figure 1). All other earthquakes occur on the four fault planes (green lines in Figure 1) with different fault geometries (Table

1). Among them, SAF and HWD correspond to the San Andreas and Hayward faults, while HWD2 and OBL are hypotehtical faults that introduce more variances in fault geometry. Each of the four faults has one M7, five M6, 52 M5, and 52 M4 rupture areas that are uniformly distributed with the goal being to sample as many of the propagation paths from the M7 rupture area as possible using the smaller events (Figure 2).

Table 1. Fault geometry in ground motion simulation

Fault	Strike	Dip	Rake
SAF	136°	85°	180°
HWD	144°	90°	180°
HWD2	144°	65°	180°
OBL	55°	70°	135°

For each M6 and M7 rupture area, 9 and 42 source realizations (i.e., hypocenter and rupture variations) are created, respectively. For each M4 and M5 rupture area, only one rupture variation is created, because finite-fault effects are negligible on such a small rupture area for the frequency bandwidth (f<1 Hz) we are considering. Rupture areas are determined using the relation of Wells and Coppersmith (1994) and the rupture generator used in the simulation is GP15.4 (Graves and Pitarka, 2016). The waveform propagation code is from Graves (1996). We conduct two sets of simulations, one with a 1D velocity model for the Loma Prieta region (Graves and Pitarka, 2010) and one with the USGS Bay Area 3D velocity model v08.3.0 (Brocher, 2005). A minimum shear wave velocity of 500 m/s is used for both velocity models and the maximum resolved frequency of the simulations is 1 Hz.

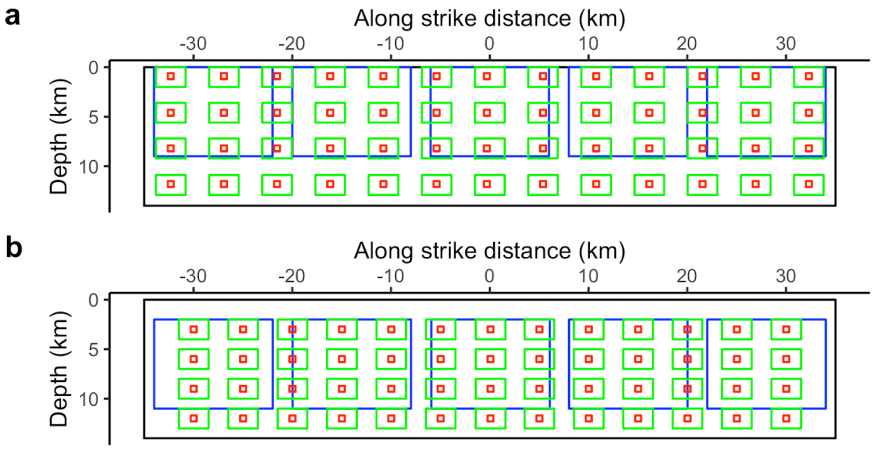

Figure 2. (a) Cross-section view of SAF and HWD. Red, green, blue, and black rectangles denote the rupture areas for M4, M5, M6, and M7 events, respectively. (b) Same for OBL and HWD2.

2.2 Non-ergodic GMM development

We first perform the linear regression with a simple functional form following Meng et al., (2023):

$$\ln(y) = b_1 + b_2 M + b_3 M^2 + (b_4 + b_5 M) \times \ln\left(\sqrt{6^2 + R_{rup}^2}\right) + b_6(1 - 0.06 Z_{TOR}) + b_7 \ln(V_{S30}) + b_8 \ln\left(\frac{Z_1}{Z_{1,ref}}\right) \quad (1)$$

where M is the magnitude; R_{rup} is the rupture distance; Z_{TOR} is the depth to the top of the rupture area; V_{S30} is the time-averaged V_S to 30m depth; Z_1 is the depth to V_S =1km/s. The V_{S30} and Z_1 terms are only used for the 3D simulation. Next, the total residuals δ are decomposed into three terms with the mixed effects regression (Bates et al., 2015): event term (δet), site term ($\delta S2S$), and within-site residuals (δWS):

$$\delta = \delta et + \delta S2S + \delta WS \quad (2)$$

In the non-ergodic GMM framework (Al Atik et al., 2010), *δWS* are regarded as the sum of the path effects and their aleatory variations.

2.3 Rupture directivity parameters

In order to systematically analyse rupture directivity's impacts on the path effects, we define several rupture directivity parameters as shown in Figure 3. θ_D is the azimuth angle from the forward rupture direction to the epicenter-site direction. θ_D=0° and ±180° represent the forward and backward rupture direction, respectively. θ_D=±90° represent the direction perpendicular to the fault strike. We also introduce the rupture ratio, *RR*, which is the ratio between forward rupture distance (s_1) and total rupture length (*L*). *RR*=0.5 and *RR*=1.0 represent pure bi-lateral and uni-lateral earthquakes, respectively.

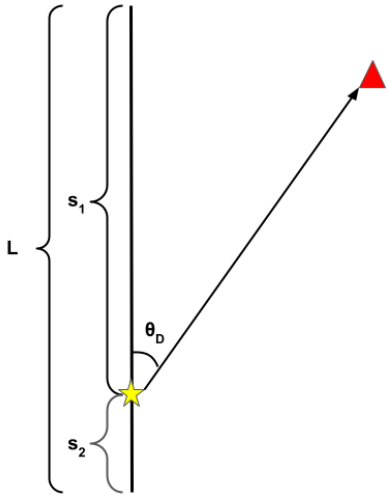

Figure 3. Schematic illustration of rupture directivity parameters. Black line denotes the surface projection of the rupture plane. Yellow star denotes the epicenter. Red triangle denotes the site. L is the total rupture length. s1 and s2 are forward and backward rupture length, respectively. θ_D is the azimuth angle from the forward rupture direction to the site.

3 Results

For brevity, in the remainder of the paper we focus on the 5s period pseudo spectral acceleration (RotD50) results from the Hayward fault (HWD) simulation using the 1D velocity model, as waveform propagation in the 1D velocity model is much simpler, which makes the identification of source and path effects in *δWS* much easier. Features seen in these results are representative of those identified in the other simulations.

3.1 Radiation pattern and rupture directivity

We first examine the variation of *δWS* with θ_D with different magnitude and *RR* groups (Figure 4). *δWS* of M4 and M5 events are dominated by the radiation pattern for all *RR* groups as indicated by the very systematic pattern of peaks and troughs as a function of θ_D. For the M6 group, *δWS* of the bi-lateral (*RR*: 0.5-0.66) events are also dominated by the radiation pattern, while *δWS* of the uni-lateral events (*RR*>0.67) show a combination of radiation pattern and forward directivity. For the bi-lateral M7 events, we observe increased *δWS* at both forward and backward rupture directions (0° and ±180°, respectively). For the uni-lateral M7 events, the forward directivity signals are evident. The observation of the significant variations of *δWS* with θ_D indicates that, in the 1D simulation, anelastic attenuation are secondary factors in modifying ground motions compared to the radiation pattern and rupture directivity.

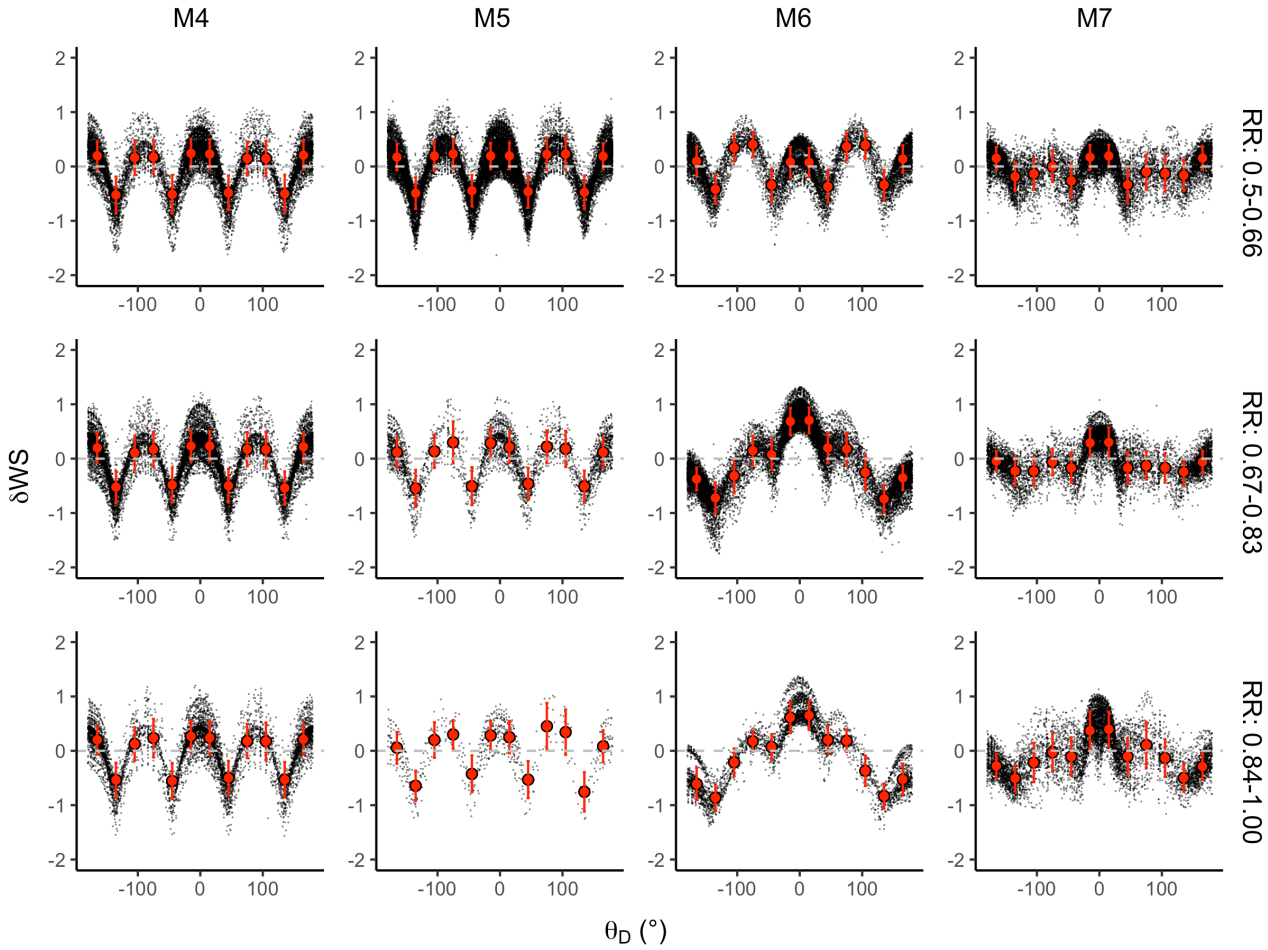

Figure 4. δWS versus θ_D for different magnitude and RR groups. Black dots denote results from the simulation. Red dots and bars denote the mean values and standard deviations, respectively.

Next, we compare the observed radiation pattern and rupture directivity effects to a published rupture directivity model (Bayless et al., 2020; hereafter BA20). Figure 5 shows the comparison between the map of *δWS* and the predicted rupture directivity pattern for a M6 event. It is evident that BA20 significantly underpredicts the observed rupture directivity in our simulation, in terms of both amplitude and affected area. In order to better fit our simulation data, we modify BA20 by removing the distance taper and replacing a simplified radiation pattern predictor with the theoretical far-field radiation pattern of a double-couple point source by Aki and Richards, (2002) (eq.3).

$$f_D(M,T,x,fault) = a(M,T,fault) + b(M,T,fault) f_{s2}(x) f_{rp}(\phi,\upsilon,\lambda,\theta,\xi) f_\phi(x,fault) \quad (3)$$

where f_D is the adjustment term for rupture directivity; f_{S2} is the predictor function for the distance the rupture has travelled towards a site, whose full expression can be found in Bayless et al., (2020); f_{rp} is the theoretical radiation pattern, whose full expression can be found in Aki and Richards (2002); f_ϕ is the azimuth predictor, whose full expression can be found in Bayless et al., (2020); *a(M, T, fault)* and *b(M, T, fault)* are magnitude-, period-, and fault-dependent intercept and slope of the rupture directivity adjustment, respectively, and are regressed over our simulation data. The fit between the observed rupture directivity and prediction from the modified model are significantly improved (Figure 6), which indicates that we could adequately remove radiation pattern and rupture directivity from *δWS*.

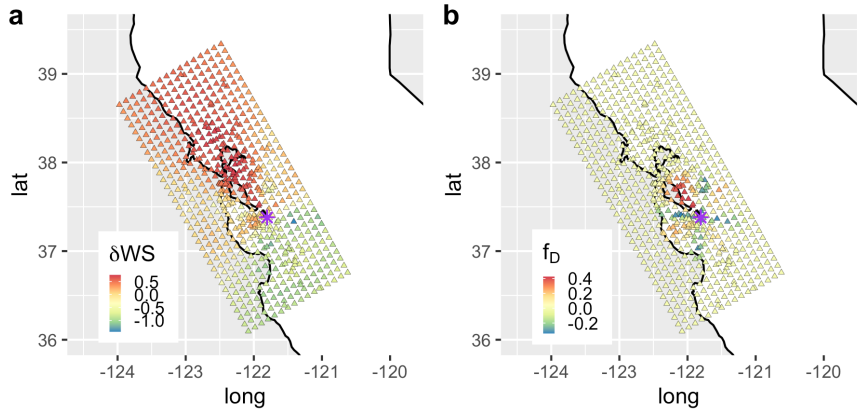

Figure 5. Map of (a) δWS and (b) rupture directivity prediction by the Bayless model for a M6 event.

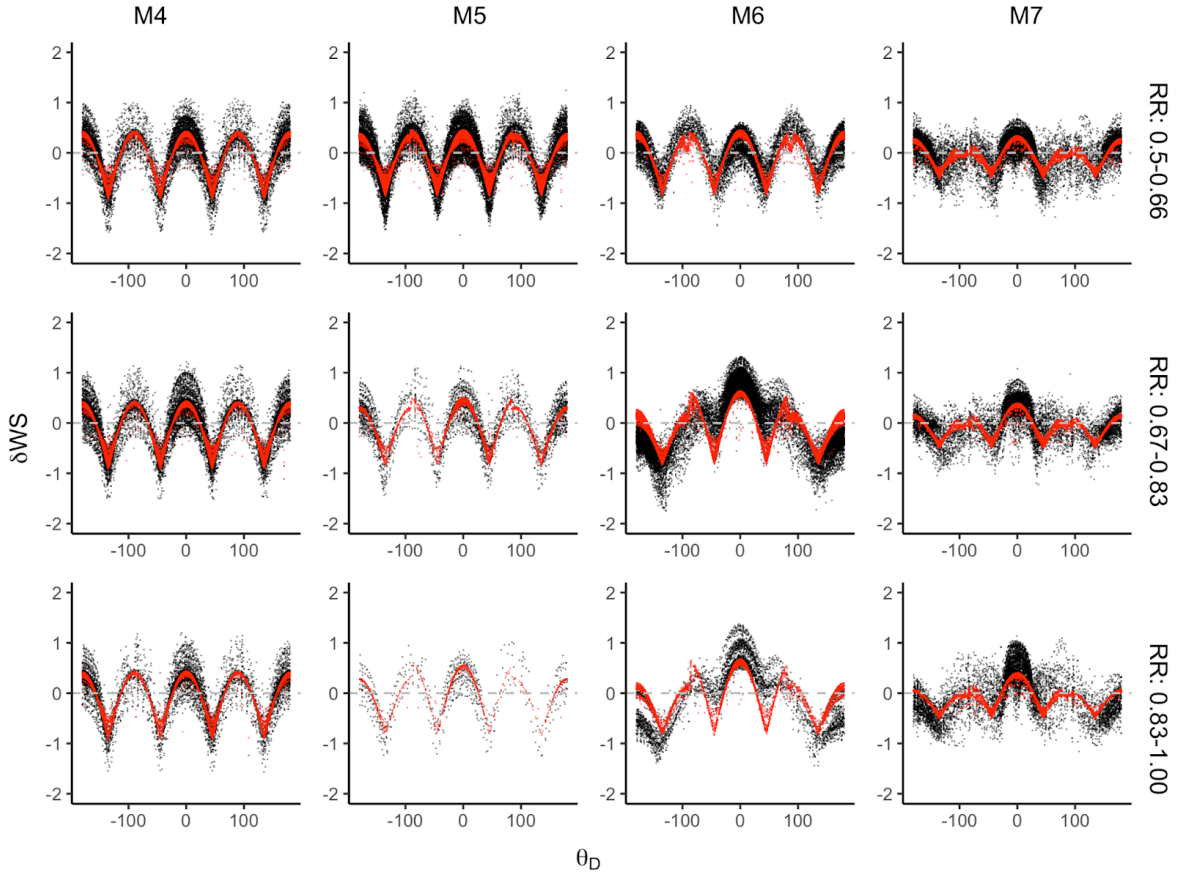

Figure 6. Comparison between observations (black dots) and predictions by the modified rupture directivity model (red dots).

3.2 Slip patterns

Another source characteristic that could affect ground motions is the slip pattern. Figure 7 shows the map of *δWS* and the slip pattern of a bi-lateral M7 event. Although we expect to observe a symmetric *δWS* pattern, the map of *δWS* shows much larger ground motions toward SE than NW (Figure 7b), which is most likely caused by a few high slip areas toward the SE end of the rupture area (Figure 7a). Motivated by this observation, we compute the standard deviation of *δWS* (σ_{WS}) at each site among M7 events with similar hypocentral locations (Figure 8). There are significant variations of *δWS* at most sites (Figure 8a-c). σ_{WS} versus θ_D shows a “M" shape (Figure 8d-f). Normal to the fault strike direction (θ_D=±90°), *δWS* are affected more significantly by slip patterns than along the strike direction (θ_D=0° or ±180°). Nevertheless, it is clear that slip

patterns have notable effects on ground motions, and can outweigh the radiation pattern and rupture directivity in some cases.

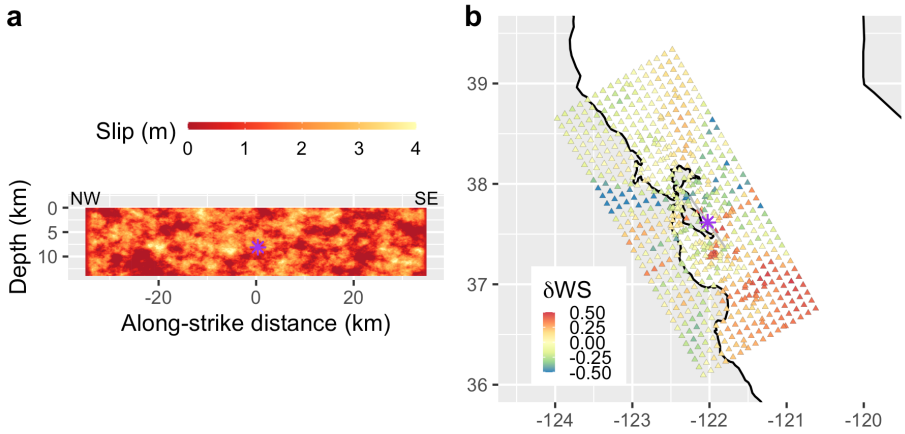

Figure 7. (a) Cross-section view of slip pattern for a M7 event. Purple star denotes the hypocenter. (b) Map of δWS. Gray line and purple star denote the surface projection of the fault plane and epicenter of the M7 event, respectively.

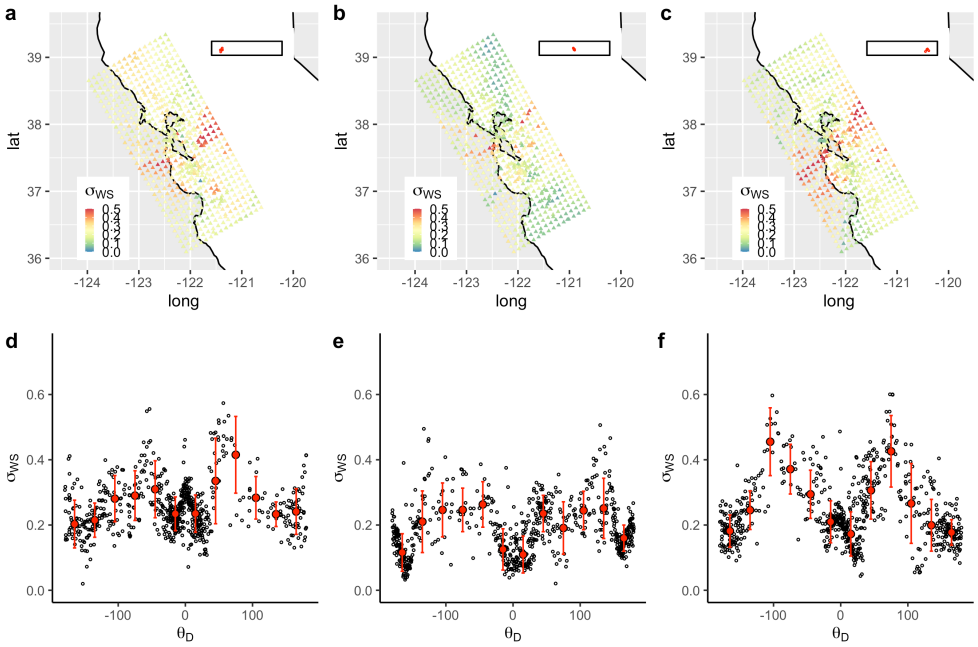

Figure 8. (a-c) Maps of σ_{WS} for three groups of M7 events with similar hypocentral locations. The inset rectangle at the top-right corner denotes the cross-section view of the rupture plane. The red dots denote the hypocenters. (d-f) σ_{WS} versus θ_D for three groups of M7 events (black dots). The red dots and bars denote the mean values and standard deviations.

3.3 Path term comparison

Finally, we compare the path terms for a site *s* computed with different magnitude groups *M* ($\delta P2P_{M,s}$), after our attempt to remove the radiation pattern and rupture directivity from *δWS*. Since our simulation includes multiple rupture variations for each M6 and M7 rupture area, the effects of slip patterns can be minimized by averaging among the rupture variations. We use two approaches to compute $\delta P2P_{M,s}$ for each magnitude group. For the first approach, we compute $\delta P2P_{M,s}$ using events in a magnitude group that have the shortest path to site *s* only (Figure 9 and eq.4).

$$\delta P2P_{M,s} = \sum_{i=1}^{N_r} \frac{\delta WS_{i,s} - f_D^{i,s}}{N_r} \quad (4)$$

where *i* is the index of events on the rupture plane *r*, which has the shortest path to site *s* from the magnitude group *M*, N_r is the number of events on the rupture plane *r*, $\delta WS_{i,s}$ is the within-site residual from event *i* to site *s*, and $f_D^{i,s}$ is the predicted radiation pattern and rupture directivity from event *i* to site *s* by the modified model. This represents the current approach of computing the path effects in non-ergodic GMM development. For the second approach, we compute $\delta P2P_{M,s}$ using all events in the magnitude group *M*, whose contributions are inversely weighted by R_{rup} (Figure 9 and eq.5).

$$\delta P2P_{M,s} = \sum_{i=1}^{N_M} \frac{(\delta WS_{i,s} - f_D^{i,s}) * \min(R_{rup}^{i,s})}{N_M * R_{rup}^{i,s}} \quad (5)$$

where *i* is the index of events from the magnitude group *M*, N_M is the number of events from the magnitude group *M*, and $R_{rup}^{i,s}$ is the rupture distance from event *i* to site *s*. Hereafter we referred the first and second approach as the shortest path and the aggregation approach, respectively.

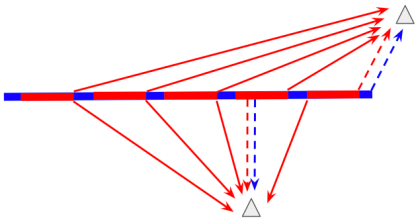

Figure 9. Schematic illustration of the two approaches for computing δP2P. Grey triangles denote sites. Blue and red rectangles denote the surface projection of rupture panes for large and small events, respectively. Dashed blue and red lines denote the shortest path to a site for large and small events, respectively. Solid red lines denote all paths other than the shortest path for small events.

Using the shortest path approach, we observe good correlation of $\delta P2P_{M,s}$ between M4 and M5 events only (Figure 10), which are essentially co-located point sources. The correlation coefficients of $\delta P2P_{M,s}$ between any other two magnitude groups are very close to zero (Figure 10). Using the aggregation approach, the correlation coefficients of $\delta P2P_{M,s}$ between any two magnitude groups noticeably improves (Figure 11). However, other than between M4 and M5, the correlation coefficients computed with the aggregation approach do not exceed 0.5, which suggests that $\delta P2P_{M,s}$ computed from different magnitude groups still have large differences.

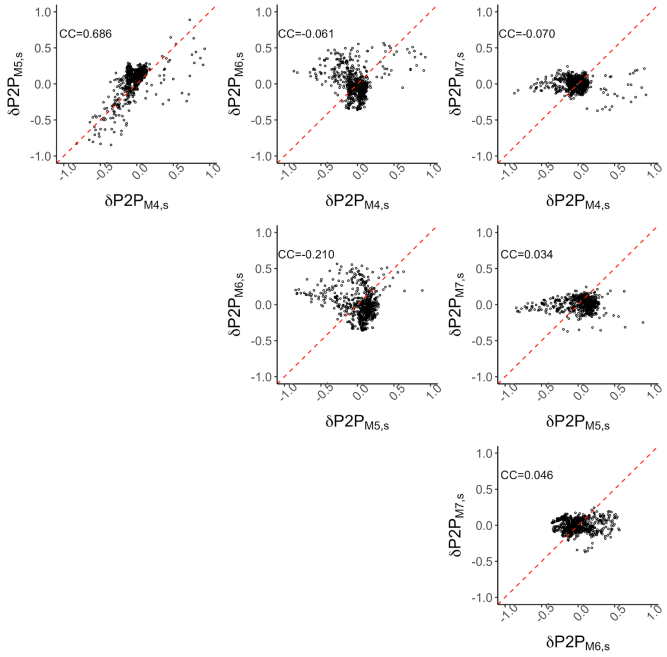

Figure 10. Comparison of δP2P computed with the shortest path approach between two magnitude groups. CC is the computed correlation coefficient for the data points.

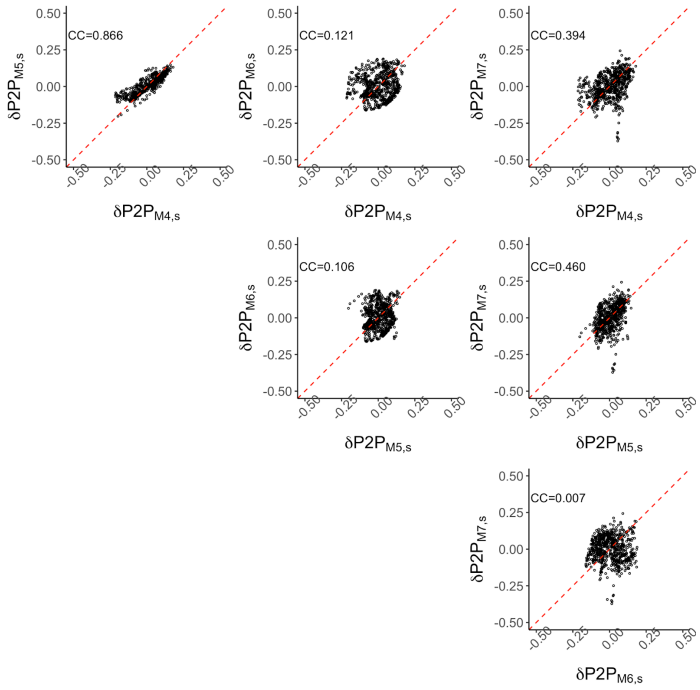

Figure 11. Comparison of δP2P computed with the aggregation approach between two magnitude groups.

4 Discussion

In our simulations using a 1D velocity model, we find strong radiation pattern and rupture directivity. The relative importance of the radiation pattern to rupture directivity decreases with magnitude. For M4 and M5 events, there is only radiation pattern in *δWS.* There are combined effects of radiation pattern and uni-lateral directivity for M6 events. For M7 events, bi-lateral and uni-lateral directivity are observed. We also find that slip patterns can have significant impacts on the ground motions, which can obscure the radiation pattern and rupture directivity effects in certain cases. Compared to those source effects, the wave propagation effects along the travel path are only secondary factors. Therefore, if we want to extract the genuine path effects from the simulation, we must first remove the effects of radiation pattern, rupture directivity, and slip patterns.

The 1D simulation produces stronger rupture directivity in a much wider area than predicted by BA20. The observed rupture directivity can be better fitted by a modified rupture directivity mode, in which the distance taper in BA20 is removed and coefficients are regressed over the simulation data. Furthermore, the effects of slip patterns on the rupture directivity are negligible due to the averaging among multiple rupture variations for the rupture area. Even after removing the effects of radiation pattern, rupture directivity, and slip patterns, we find that $\delta P2P_{M,s}$ computed with the shortest path approach still have large discrepancies between different magnitude groups. In non-ergodic GMM development with empirical data, it is often assumed that $\delta P2P_{M,s}$ between small and large events are the same, as long as they have the same shortest path to the site. Our results suggest that such assumption is not appropriate, most likely due to the fact that large events can no longer be treated as point sources and the shortest path does not adequately represent the genuine wave propagation path. To remove this assumption, we compute $\delta P2P_{M,s}$ with the aggregation approach, which considers all possible paths from the rupture plane of the large events. Although the correlations of $\delta P2P_{M,s}$ indeed improve notably for many cases, the correlation coefficients are still too low to claim that the path effects of large events can be approximated by that of small events. The poor correlations are likely due to the more subtle signals of wave propagation being obscured by effects including residuals of the modified rupture directivity model, reflected waves at both Moho boundary and free surface, and monochromatic surface waves trapped in the shallow layers in the 1D velocity model. Note that while the latter two effects are related to the propagation path, they are manifest differently and over different distance ranges for small compact sources compared to large extended ruptures, hence making it difficult to account for their behavior even with the aggregate approach.

Our analysis so far focuses on HWD at 5s in the 1D simulation only. The main findings of strong source effects in *δWS* are consistent across different periods, but the details vary. For example, Figure 12 shows *δWS* versus θ_D for HWD at 10s in the 1D simulation. The main differences at 10s are that the radiation pattern is more prominent for M6 events, and the rupture directivity of M7 events becomes stronger. Overall, we observe that the period of the strongest rupture directivity is closely related to the rupture length, that is, longer rupture length produces the strongest rupture directivity at longer periods.

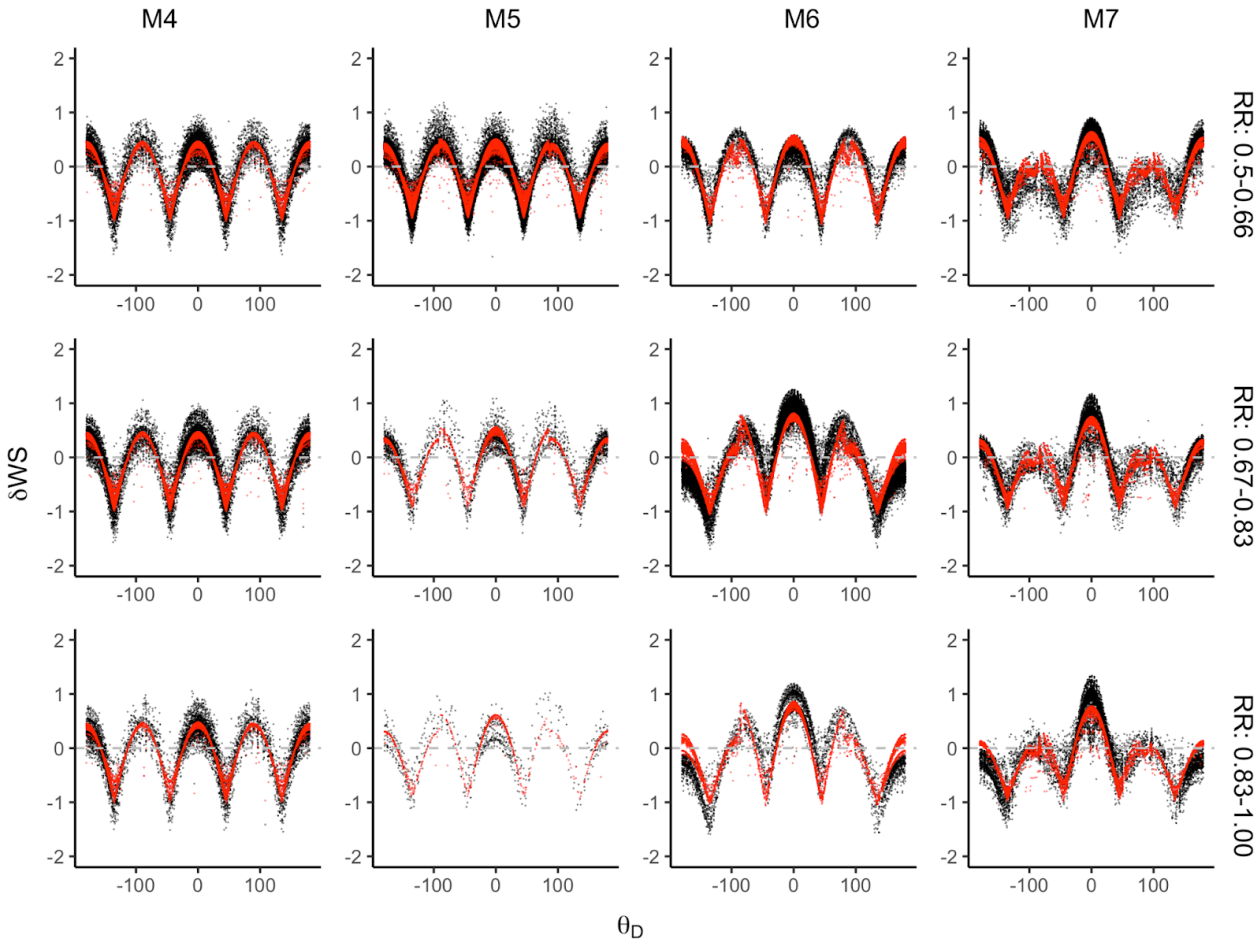

Figure 12. Comparison between observations (black dots) and predictions by the modified Bayless model (red dots) at 10s.

We also investigate the results for HWD at 5s in the 3D simulation (Figure 13). The radiation patterns from M4 and M5 events still dominate *δWS*, but with much larger variations than the 1D simulation, which are caused by the strong scattering of the 3D velocity model. Similarly, rupture directivity is still evident for M6 and M7 events in the 3D simulation; however, it is not as well defined as in the 1D simulation due to the more complicated wave propagation in the 3D simulation. Furthermore, the modified rupture directivity model developed in this study can be utilized to better account for radiation pattern and rupture directivity effects when utilizing CyberShake results to analyse region-specific path effects, which used the same rupture generator as in our simulation (Graves et al., 2011).

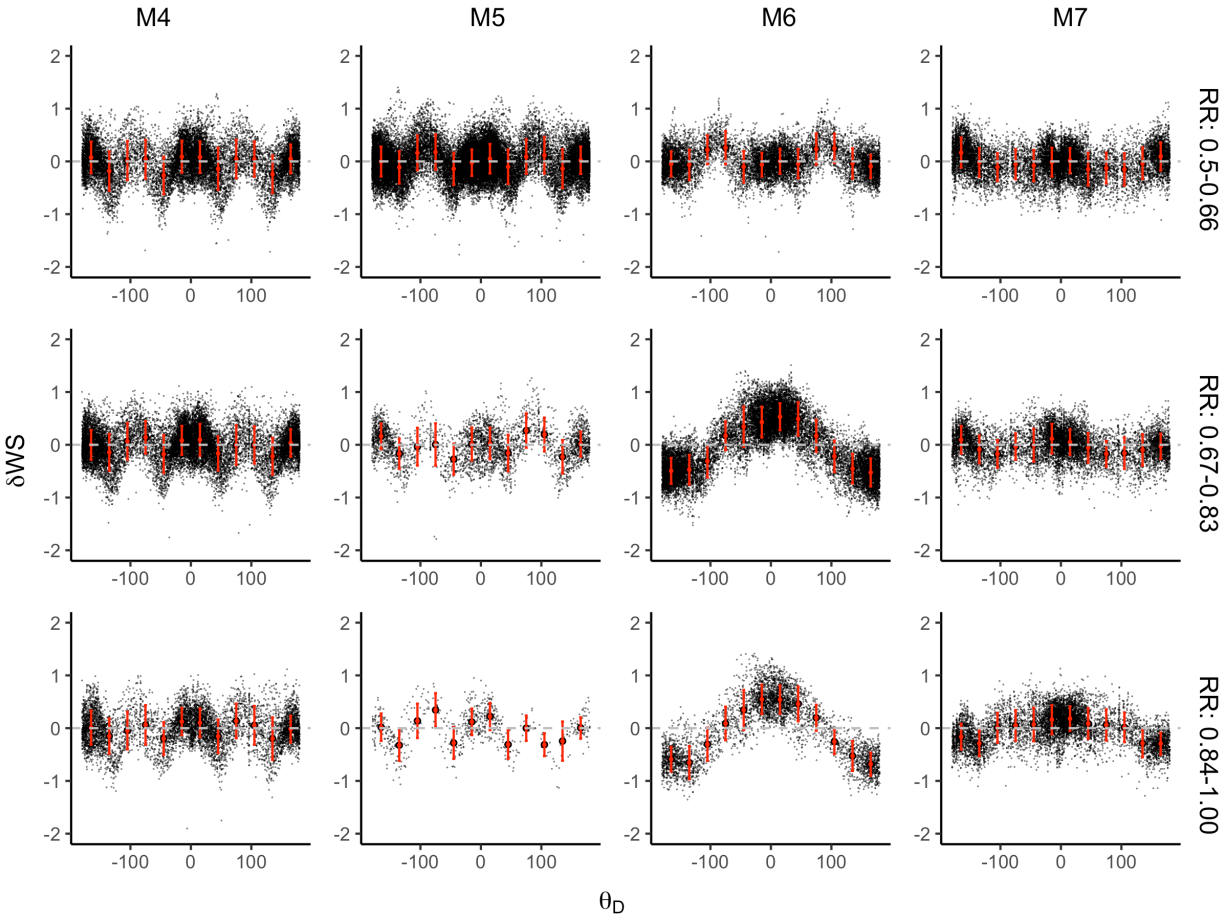

Figure 13. Comparison between observations (black dots) from 3D simulation and predictions by the modified Bayless model (red dots) at 5s.

5 Conclusions

We find that source effects like radiation pattern, rupture directivity, and slip patterns have profound impacts on the ground motion in our simulations. Since those impacts depend on the location of both the source and site, they can be mapped into path effects during the non-ergodic GMMs development, which introduces significant bias in path-specific seismic hazard analysis. The radiation pattern and rupture directivity on vertical strike-slip faults can be fit reasonably well by a modified rupture directivity model based on BA20. After removing the modelled rupture directivity and minimizing the effects of slip patterns by including multiple realizations per rupture area, we compare the path effects computed with small and large events. Using the approach that only considers the events with the shortest path to a site in a magnitude group, we observe little correlation between path terms computed with small and large events, suggesting the assumption of same path effects for all magnitudes in current non-ergodic GMM development is flawed. The path terms aggregated over all small events that cover the entire rupture area of a large event have better correlations with that computed with large events. However, the correlation coefficients are still too low to fully approximate the path effects of large events with that of small events. The poor correlations are likely caused by deficiencies of the rupture directivity model, as well as reflected waves and trapped surface waves, which have different characteristics for small magnitude events compared to large magnitude (extended rupture) events. Results from this study not only provide guidance in extracting path effects from CyberShake studies, but also serve as a reminder to other scientists and engineers working on developing non-ergodic GMMs with either simulation or empirical data, that it is critical to investigate the significance of source effects and their impacts on the path effects. Observations in this study are primarily from a vertical strike-slip fault in the 1D simulation at 5s, which may be significantly different for other focal mechanisms, velocity models, and periods. Therefore, we will conduct more comprehensive investigations on our results' dependency on focal mechanisms, velocity models, and periods in a future study.

6 References

Aki, K. and Richards, P.G. (2002). Quantitative Seismology. University Science Books.

Al Atik, L. et al. (2010). The Variability of Ground-Motion Prediction Models and Its Components, Seismological Research Letters, 81(5), pp. 794–801.

Bates D, Mächler M, Bolker B, Walker S (2015). "Fitting Linear Mixed-Effects Models Using lme4." *Journal of Statistical Software*, 67(1), 1–48. doi:10.18637/jss.v067.i01.

Bayless, J., Somerville, P. and Skarlatoudis, A. (2020). A Rupture Directivity Adjustment Model Applicable to the NGA-West2 Ground Motion Models and Complex Fault Geometries, United States Geological Survey Report.

Brocher, T.M. (2005). Compressional and shear wave velocity versus depth in the San Francisco Bay Area, California: rules for USGS Bay area velocity model, United States Geological Survey Report.

Graves, R. W., and A. Pitarka (2010). Broadband ground-motion simulation using a hybrid approach, Bull. Seismol. Soc. Am. 100, 2095–2123, doi: 10.1785/0120100057.

Graves, R. et al. (2010). CyberShake: A Physics-Based Seismic Hazard Model for Southern California, Pure and Applied Geophysics, 168(3), pp. 367–381.

Graves, R. and Pitarka, A. (2016). Kinematic ground-motion simulations on rough faults including effects of 3D stochastic velocity perturbations, Bulletin of the Seismological Society of America, 106(5), pp. 2136–2153.

Graves, R.W. (1996). Simulating seismic wave propagation in 3D elastic media using staggered-grid finite differences, Bulletin of the Seismological Society of America, 86(4), pp. 1091–1106.

Meng, X., C. Goulet, K. Milner and S. Callaghan (2023), Comparison of Nonergodic Ground Motion Components from CyberShake and NGA-West2 Datasets in California, Bulletin of Seismological Society of America, doi: https://doi.org/10.1785/0120220049.

McGuire, R.K. (1995). Probabilistic seismic hazard analysis and design earthquakes: Closing the loop, Bulletin of the Seismological Society of America, 85(5), pp. 1275–1284.

McGuire, R.K. (2004) Seismic Hazard and Risk Analysis. Earthquake Engineering Research Institute.

Strasser, F.O., Abrahamson, N.A. and Bommer, J.J. (2009). Sigma: Issues, Insights, and Challenges, Seismological Research Letters, 80(1), pp. 40–56.

Wells, D. L., and K. J. Coppersmith (1994). New empirical relationships among magnitude, rupture length, rupture width, rupture area, and surface displacement, Bulletin of the Seismological Society of America 84, 974–1002, doi: 10.1785/BSSA0840040974